36

Implications of Crustal Strain During Conventional, Slow, and Silent Earthquakes

M.J.S. Johnston
US Geological Survey, Menlo Park, USA
A.T. Linde
Carnegie Institution of Washington, Washington, USA

1. Introduction

Uniform block-slip motion consistent with simple shear on locked fault segments is the primary feature apparent in geodetic measurements of strain accumulation along plate boundaries (Savage, 1983). However, almost every aspect of fault failure is nonlinear in character. This premise derives from theoretical models (Kostrov, 1966; Richards, 1976; Andrews, 1976; Freund, 1979; Rice and Rudnicki, 1979; Rice, 1983, 1992; Stuart, 1979, Stuart and Mavko, 1979; Das and Scholz, 1981; Rundle *et al*., 1984; Tse and Rice, 1986; Lorenzetti and Tullis, 1989; Segall and Rice, 1995; Shaw, 1997; Miller *et al*., 1999) and laboratory-generated frictional failure of crustal materials (Dieterich, 1979, 1981; Mogi, 1981; Mogi *et al*., 1982) which predict accelerating deformation will occur before dynamic slip instabilities, better known as earthquakes.

To investigate this physics of fault failure, it has increasingly become obvious that new techniques, with capability to resolve strain at better than 1 part per billion (ppb), are needed. Geodetic and GPS strain measurements with resolutions with approximately 0.4 parts per million (ppm) resolution on 5-km baselines may help with some broadscale problems such as fault interaction, viscoelastic response (Thatcher, 1983; Pollitz *et al*., 1998), coseismic and postseismic response of large earthquakes (Langbein *et al*., 1983; Bock *et al*., 1997; Burgmann *et al*., 1997), but issues regarding the type of slip transients, the relative frequency of slip transients, fault creep, earthquake nucleation, pore pressure changes, slow earthquakes and silent earthquakes (where moment release is usually below that typically released for a $M = 5$ earthquake), are unlikely to be resolved with these techniques. Some strain transients, such as those occurring postseismically have been known for a long time (e.g., Langbein *et al*., 1983; Thatcher, 1983). Many others, including those occurring aseismically, are not well documented or understood even though they may play important roles in the fault-failure process.

From previous strain studies (Johnston *et al*., 1987; Wyatt, 1988), and discussed further here, it is now generally clear that entire rupture zones do not exhibit nonlinear behavior as implied by “preparation zone” terminology (Sadovsky *et al*., 1972) and some theoretical models of the rupture process (Mjachkin *et al*., 1975; Tse and Rice, 1986). Nonlinear (accelerating) deformation is not apparent in arrays of sensitive strain and tilt instruments installed throughout regions that have subsequently ruptured. Instead, rupture over a large fault length appears to be triggered by failure of smaller regions with higher strength, and this rupture draws on the elastic strain energy in the region. The expected signals should have occurred during the period immediately preceding rupture initiation. Also, the total slip moment (preseismic, coseismic, and postseismic) could be determined when each phase of the rupture process is identified.

If failure initiates in small regions of high strength and expands to any arbitrary size until stopped by another mechanical or geometrically strong barrier, this failure still has an easily identifiable form (nonlinear exponential-like strain increase). Unfortunately, detection of any preseismic slip and, more importantly, prediction of the final rupture size, will be difficult to achieve (Brune, 1979) because the total moment release during this time is only a small fraction of that released coseismically.

The timescale of failure is also not clear although the absence of obvious tidal triggering (Heaton, 1982) implies the final stage of failure occurs at periods comparable to, or

Copyright © 2002, Elsevier Science Ltd. All rights of reproduction in any form reserved.

shorter than, the major earth tidal periods (12.42, 23.93, 25.82 h, etc.). Numerous observations (Rikitake, 1976; Mogi, 1985) indicate cases when this appears to be true. The shortest timescale for nonlinear strain can be estimated from subcritical crack growth in brittle materials (Atkinson, 1979). However, it is expected that the presence of fluids should stabilize and slow down the process of cascading crack fusion in rock at the temperatures and pressures expected in the upper 10 km of the Earth's crust (Rice and Rudnicki, 1979), as shown in Figure 1. Strain during the final stages before failure accelerates dramatically in comparison with earlier periods, with maximum strain occurring, as expected, at the point of rupture.

Laboratory experiments also indicate that these last stages of failure of crustal rock (sometimes termed tertiary creep) are the end result of a process of cascading crack coalescence which results in strain time histories similar to those shown in Figure 1 (see, for example Mogi, 1985). Large-scale laboratory models with preexisting artificial faults, either with or without gouge material, exhibit similar behavior (Dieterich, 1979; Mogi, 1981, 1985; Mogi *et al*., 1982).

If the timescale of failure initiation is between one second and one day, continuous measurements of the state of strain and tilt in the Earth's crust near moderate to large earthquakes should quickly provide detailed information on time history, failure mechanics, and size (moment) of the prerupture failure. This assumes, of course, that these measurements are recorded at a sensitivity sufficient to detect failure nucleation in the last few hours to seconds before rupture occurs.

Observations of crustal strain at high sensitivity near large earthquakes during the final stages before rupture are unfortunately rare, and knowledge of the timescale and mechanics of failure is therefore limited. This has resulted largely from the infrequency of earthquakes and the poor areal coverage with adequate instrumentation. With the installation of borehole strain and tilt arrays along the San Andreas fault system and in other seismically active places during the last ten years, data are now accumulating. Along the San Andreas fault, many events have occurred for which we have near-field recordings at high sensitivity although only two for which the magnitude was greater than 7. In addition, we can call upon events recorded with similar instruments in Japan (e.g., Sacks *et al*., 1978, 1979) and Iceland (Linde *et al*., 1993).

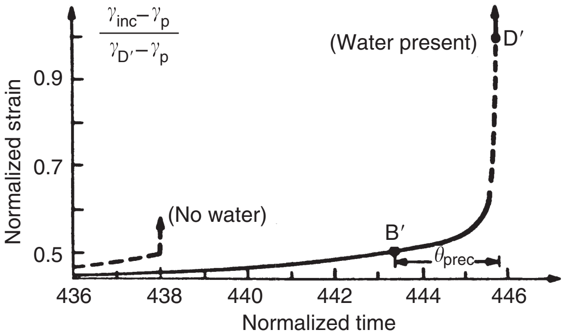

FIGURE 1 Normalized strain time history arising from fault instability models with and without the presence of water (from Rice and Rudnicki, 1979). Θ_{prec} refers to the precursor time defined by Rice and Rudnicki (1979). B′ is the onset of instability, D′ is the onset of dynamic instability and the dashed portions of the curves indicate where the numerical calculations were truncated.

In this paper we use these data to: (1) document the implications of crustal strain observed during fault creep events; (2) compare the expected form of slip waves on active faults with observations of crustal strain recorded near these faults; (3) compare the coseismic strain generated by earthquakes with calculations from simple elastic dislocation models of the events derived from seismic observations to determine the ratio of total moment release to seismic moment release; (4) discuss some observations of "slow" and "silent" earthquakes, and finally, look at the state of strain during the last few hours to the last few seconds before earthquakes and the implications this has for the issue of earthquake nucleation, earthquake prediction, and current theory. In particular, we use these strain observations to estimate the maximum preseismic slip moment release as a fraction of the observed seismic moment release and to place upper limits on nucleation source size.

2. Experimental Design and Measurement Precision

2.1 Basic Measurement Limitations

Strain measurements have historically been made along active faults using long baseline geodetic techniques. Sampling was approximately annual and the sensitivity was about 1 ppm. Unfortunately, these techniques lack the sensitivity required to detect short wavelength (5 km) slip waves propagating along faults, coseismic strains for earthquakes with $M \leq 5$, details of aseismic slip, slow earthquakes, and silent earthquakes. New arrays of GPS instrumentation will improve observations of secular motions because of their increased spatial coverage but the sensitivity in the critical band from months to milliseconds is still several orders of magnitude worse than that attainable with borehole strainmeters. Figure 2 shows the comparative resolution of the different measurement techniques as a function of period. Near-surface strainmeters always had more short-term sensitivity than geodetic observations but did not have the long-term stability or spatial averaging to determine long-term strain rates. Records were also compromised at times by effects of rainfall (Wolfe *et al*., 1981; Yamauchi, 1987). Lower-noise strain data were sometimes obtained by placing strainmeters in deep tunnels and mines. However, a real breakthrough resulted when strainmeters were installed in deep boreholes far from surface noise sources.

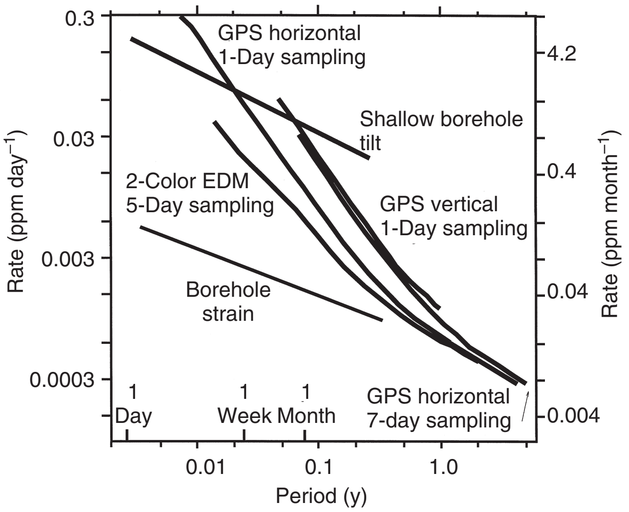

FIGURE 2 Comparative resolutions of crustal strain rates for borehole strainmeters, differential GPS, EDM and tilt sensors as a function of period (after Langbein and Johnston, 1996). (Note: GPS and EDM strain assume an 8 km baseline.)

Figure 3a shows strain noise spectra for different depths of burial. At a depth of burial of 200 m noise spectra from strainmeters in a variety of geophysical environments are identical within the errors. Figure 3b shows that the same spectra are obtained whether the strainmeter is in a volcanic region (POPS), within a few hundred meters of a currently quiescent but active region of the San Andreas fault (PUBS), or near a creeping fault (GH2S). Similar spectra are obtained at other sites either near to, or many tens of kilometers from the San Andreas fault.

2.2 Experimental Techniques

The location of the various borehole strainmeters along the San Andreas fault in California is shown in Figure 4. The borehole strainmeters shown as black dots measure dilatational strain (Sacks *et al*., 1971), whereas those shown as black squares measure 3-component or tensor strain (Gladwin, 1984; Gladwin *et al*., 1987). The sensitivities of the dilatometer and tensor strainmeters are less than 10^{-11} and less than 10^{-9}, respectively. Each of the strain sensors is installed at depths between 100 and 200 m and each detects strains at levels at least 20 dB below those obtained on near-surface strainmeters (Johnston and Borcherdt, 1984). The dynamic range exceeds 140 dB (Sacks *et al*., 1971; Sacks, 1979; Gladwin, 1984) over the period band of 0.1 sec to several months. During installation, the strain sensors are cemented in the borehole with expansive grout. The borehole is then filled to the surface with cement to avoid long-term strains from hole-relaxation effects and re-equilibration of the aquifer system.

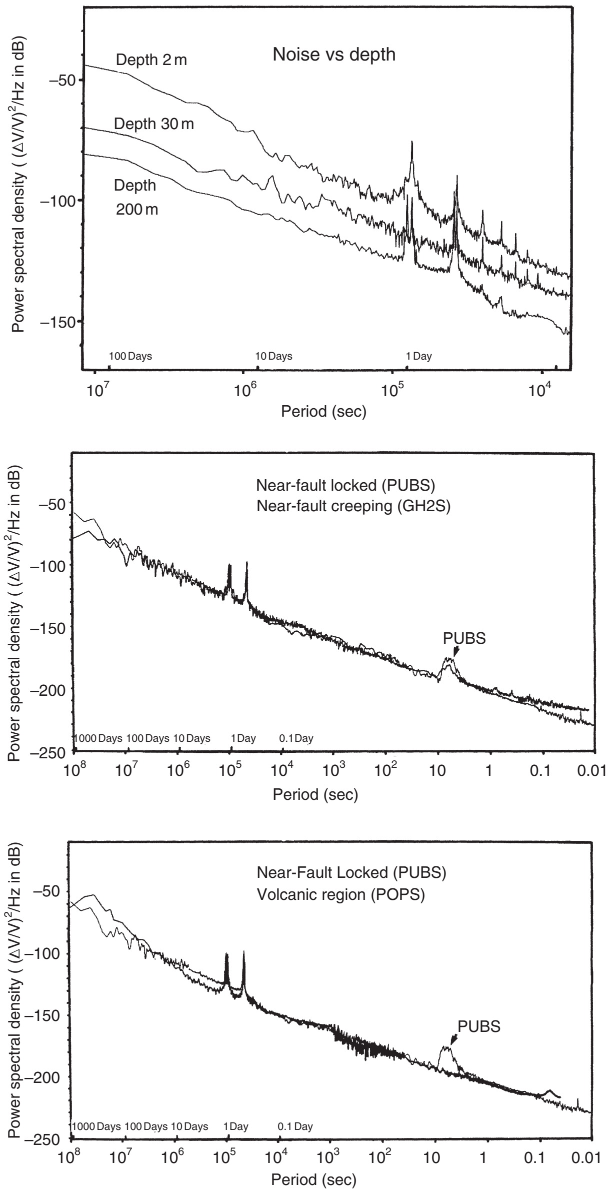

FIGURE 3 (a) Strain noise power and a function of depth beneath the Earth's surface. (b) Comparative strain noise power over ten decades of frequency for different sites in California. PUBA is within 500 m of the San Andreas fault in southern California, GH1S is within 1 km of a creeping segment of the San Andreas fault near Parkfield, and POPA is near an active volcanic caldera in eastern California.

These broadband instruments record data over ten decades of frequency. Strain from atmospheric pressure loading of the Earth's surface and from the solid earth tides (including effects from ocean loading) are the most obvious signals continuously evident in the data. Superimposed on these are straingrams from local and teleseismic earthquakes. Atmospheric pressure, earth tide and ocean loading effects can be readily predicted and removed from the data (Rabbel and Zschau, 1985; Tamura *et al*., 1991; Agnew, 1997). Although other corrections, such as for the distortion of strain fields due to nearby extreme topography are sometimes necessary (Harrison, 1976), strain

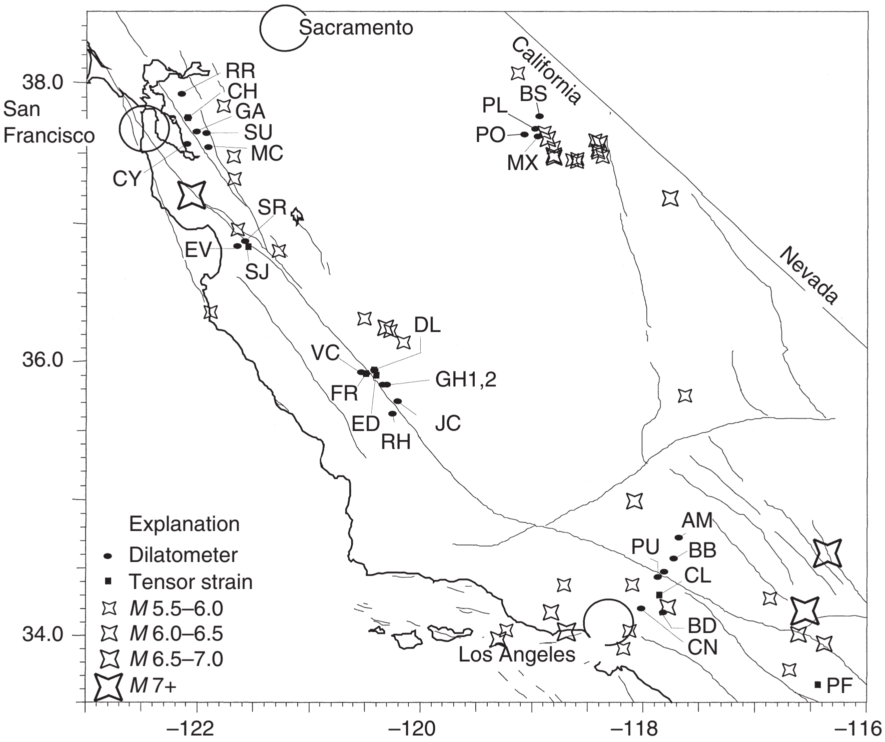

FIGURE 4 Borehole crustal strain sites in California and moderate earthquakes with magnitudes greater than 5 (shown as stars) that were recorded at these sites.

can generally be modeled with dislocations in elastic or viscoelastic half-space (Matsu'ura and Tanimoto, 1980; Okada, 1985, 1992; McTigue and Segall, 1988).

Data from these strain instruments are transmitted in 16-bit digital form through the GOES weather satellite to Menlo Park, California for processing (Silverman *et al.*, 1989). The strain sensors together with the sites are calibrated using ocean-load corrected earth tides (Linde and Johnston, 1989; Linde *et al.*, 1992; Hart *et al.*, 1996). This calibration is generally repeatable to within 1%.

3. Strain Fields and Geophysical Implications

3.1 Fault Creep Events

Surface observations of episodic displacement of active faults are usually termed fault-creep events. These creep events on the San Andreas might be argued to be a special form of slow earthquakes. However, previous work (Johnston *et al.*, 1976, 1977; McHugh and Johnston, 1977, 1978, 1979; Goulty and Gilman, 1978; Evans *et al.*, 1981; Gladwin *et al.*, 1994) indicates that the event-like nature of fault-creep events results primarily from complex failure of the near-surface fault zone materials at depths typically shallower than several hundred meters rather than fault failure at seismogenic depths. Earthquake shaking of the near-surface soils can also trigger creep events (Simpson *et al.*, 1988).

A network of strainmeters [dilational strainmeter (DS) and tensor strainmeter (TS)] installed at Parkfield (Fig. 5a) provides examples of the primary features of crustal strain during fault creep. One such example is the event on 6 October 1997, recorded on XVA1 and XPK1. The rupture length is limited since this event was not recorded at XTA1 just south of XPK1 nor at XMD1 to the northwest of XVA1. Its minimum dimension could be as small as 3 km (the distance between XVA1 and XPK1). If we search the strain records from the strainmeters, FRDS, DLDS, VCDS and EDTS, surrounding this section of the fault, we find a detectable strain transient above the noise only on the closest strainmeter FRDS (Fig. 5b). This signal indicates a compressive signal of about 15 nanostrain. A small negative change of about a nanostrain may have occurred on DLDS. An upper estimate of the depth of this creep event can be determined if we model the event using Okada's (1985, 1992) dislocation formulation using a length of 4 km, a displacement of 2.5 mm (observed at XVA1), and determining the likely depth that would generate a strain transient of 15 nanostrain at FRDS and less than a few nanostrain at the other sites. The lower plot on Figure 5b shows calculated strain amplitude as a function of the width of the creep event. It is apparent that the width cannot exceed a few hundred meters. Similar depths are obtained for numerous other creep events. These data support the notion

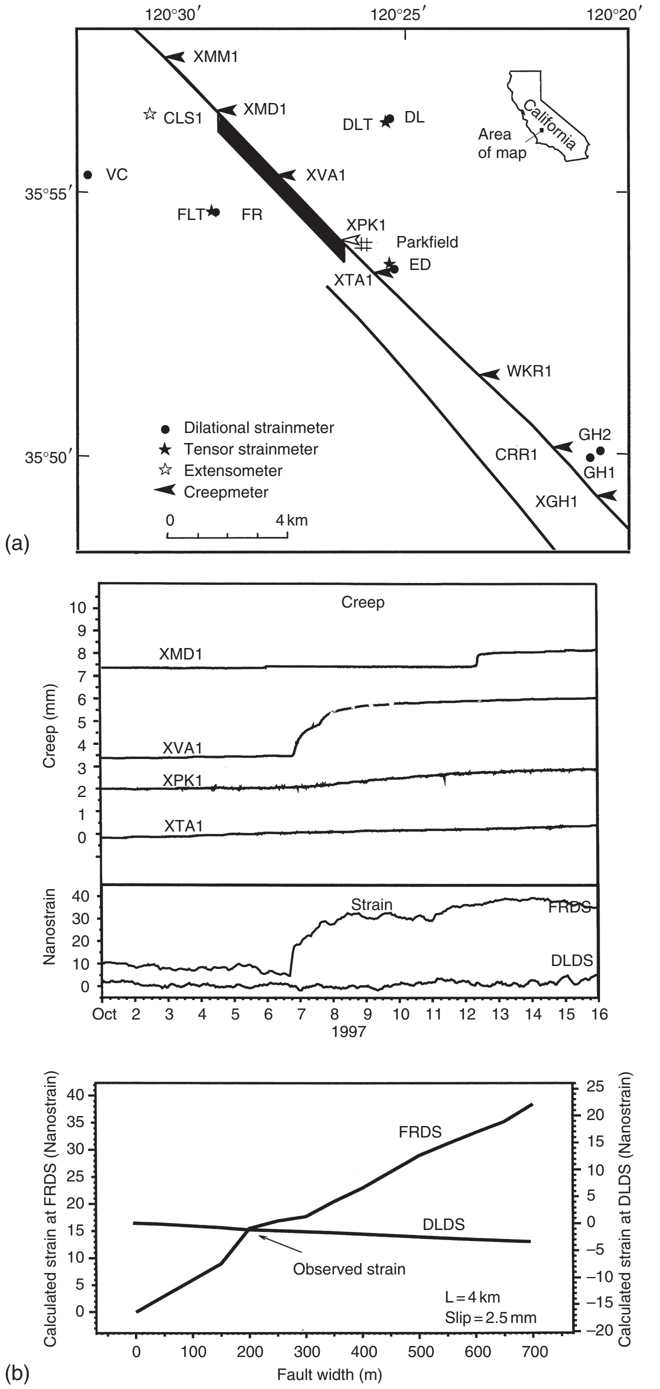

FIGURE 5 (a) Location of the dilatational strainmeters (FR, DL, JC, VC, GH1 and GH2), tensor strainmeters (FLT, DLT and EA), and creepmeters (XMM1, XMD1, XVA1, XTA1, CRR1, XPK1, XGH1, and WKR1) at Parkfield, California. The fault patch shows the location of the creep event discussed in Figure 5b. (b) Strain and creep time histories during the creep events recorded at XVA1 and XPK1 on 6–7 Oct. 1997. Creep records are shown in the top of the upper plot, strain records from FR and DL are shown in the bottom of the upper plot. The lower plot shows the calculated strain as a function of fault slip width at the two strain sites FR and DL.

that creep events result from shallow slip waves in the upper few hundred meters of the fault.

Similar conclusions were evident in data from arrays of creepmeters, strainmeters, and tiltmeters separated by only a few hundred meters in other parts of the creeping section of the San Andreas fault (McHugh and Johnston, 1979; Evans *et al.*, 1981; Goulty and Gilman, 1978). These data also indicated complexity in propagating inhomogeneous slip waves on scales of a few hundred meters. Furthermore, indications of deep slip episodes in near-fault strain data (Johnston *et al.*, 1977; Langbein, 1981; Linde *et al.*, 1996) have not been found to correspond to the times of surface creep events although the long-term fault displacement rates are mostly reflected in long-term creep rate data (Schulz *et al.*, 1982). This view of the event-like character of surface creep events is consistent with the suggestions (Marone *et al.*, 1991) that near-surface fault materials exhibit velocity strengthening but cannot ultimately sustain the rapid slip associated with earthquake source motions. In contrast, materials at seismogenic depths primarily exhibit velocity weakening as expected from theoretical work on rate and state variable friction (Ruina, 1983; Dieterich, 1994). Episodic near-surface creep events are thus not considered to be slow earthquakes.

3.2 Fault Slip Waves

The suggestion that regional strain waves may propagate along active faults has been around since the 1970s (Kasahara, 1979; Savage, 1971; Ito, 1982; Kasahara *et al.*, 1983) although little support has yet been found. Slip waves over the fault face with amplitudes of a few millimeters generate coherent strains exceeding 10^{-7} within a few kilometers of the fault. Signals of opposite form occur on opposite sides of the fault. Figure 6b shows the predicted signals on several instruments at Parkfield for a slip wave with an amplitude of 10 mm between 5 km and 10 km that propagates past several strainmeters installed within a few kilometers of the San Andreas fault, shown in Figure 6a. If these slip waves occurred with propagation velocities from kilometers per month to kilometer per minute they would be readily observable on the strainmeter arrays. Thus far they have not been seen. These slip waves could occur but not be detected on the current strainmeter arrays if the velocities are more than ten times slower (i.e., kilometers per year). Neither would these slip waves be detected in the semicontinuous two-color EDM or continuous GPS measurements in the Parkfield area unless the amplitudes were 10–100 times larger.

Nevertheless, this idea has recently resurfaced in 1995 (Press and Allen, 1995) and, again in 1998, with the suggestion (Pollitz *et al.*, 1998) that slip waves should also occur from time-dependent viscoelastic response from distant subduction earthquakes. The expected amplitudes are 10^{-8} with a timescale of several years.

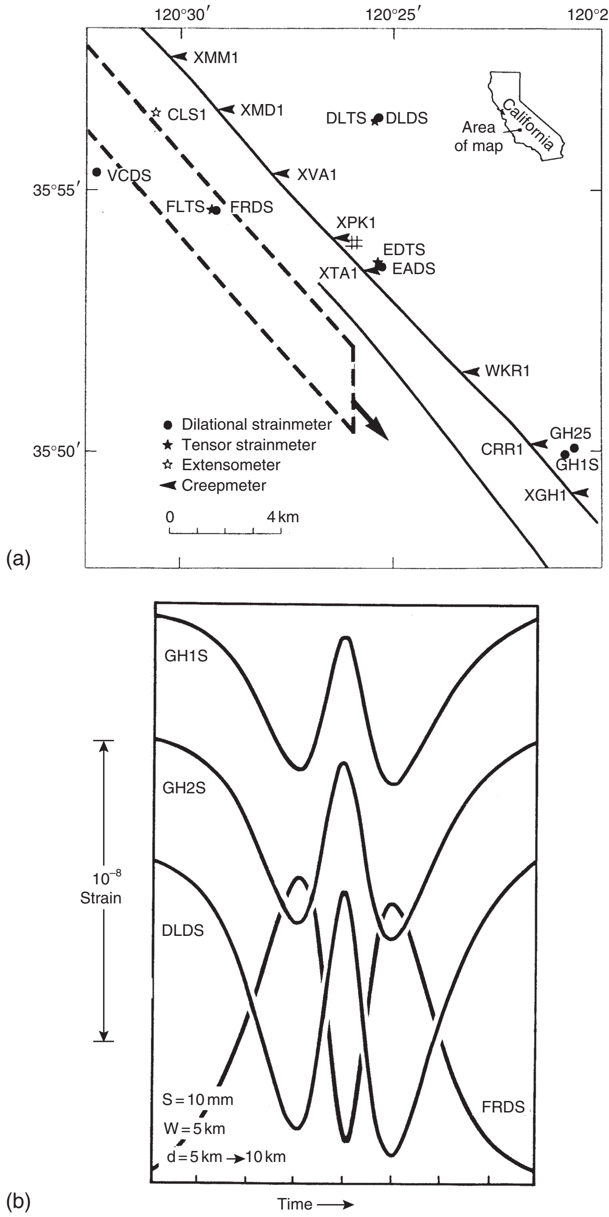

FIGURE 6 (a) Map of the Parkfield region illustrating a hypothetical slip wave propagating between 5 km and 10 km beneath the surface array of strain and creep monitoring sites. (b) Predicted strain time histories for a 5 km wide slip wave propagating between 5 km and 10 km depth past several borehole strainmeters in Parkfield. The slip amplitude is 10 mm. For clarity only four strain–time records are shown.

TABLE 1 List of earthquakes and Observed and Calculated Coseismic Strain Offsets. Details for some earthquakes were Obtained from Eaton (1985 and unpublished), Johnston *et al.* (1986), L. Jones (personal communication), Lester (persona) communication), Shimazaki and Somerville (1978), and others from the Northern California Data Center. The code name following the observed strain offsets in column 4 refers to the instrument on which the offset was observed. The locations of these instruments are shown in Figure 4

Earthquake	Magnitude	Date	Obs. Strain ($\mu\varepsilon$)	Calc. Strain ($\mu\varepsilon$)
Homestead Valley	5.2	3/3/79	1.0 (PF)	1.3
Morgan Hill	6.2	4/24/84	−72.0 (EV)?	−140.0
Morgan Hill	6.2	4/24/84	242.0 (SJI)	233.0
Morgan Hill	6.2	4/24/84	−34.0 (SJ2)	−30.0
Morgan Hill	6.2	4/24/84	192.0 (SJ3)	111.0
San Juan Bautista	3.2	5/26/84	1.9 (SR)	1.66
Kettleman Hills	5.5	8/4/84	104.0 (GHI)	108
Kettleman Hills	5.5	8/4/84	166.0 (GH2)	110
Kettleman Hills	5.5	8/4/84	342.0 (EA)	246
Round Valley	5.8	11/23/84	68.0 (PO)	45
Quiensabe	5.3	1/26/86	51.0 (SR)	39
Quiensabe	5.3	1/26/86	50.0 (SJ)	44
Mt. Lewis	5.8	3/21/86	1.5 (SR)	1.4
North Palm Springs	5.8	7/8/86	−16.6 (PU)	−10.1
North Palm Springs	5.8	7/8/86	1.0 (BB)	1.5
North Palm Springs	5.8	7/8/86	15.1 (AM)	12.3
Oceanside	5.8	7/3/86	0.6 (PU)	0.7
Chalfant	6.4	7/21/86	138.7 (PO)	122
Whittier	5.9	10/1/87	27.5 (PU)	25.2
Whittier	5.9	10/1/87	−7.1 (BB)	−6.8
Whittier	5.3	10/4/87	2.3 (PU)	2.0
Supersitition Hills	6.6	11/23/87	13.8 (PF)	13.7
Pasadena	5.0	12/3/88	−11.6 (PU)	−8.6
Sierramadre	6.0	6/28/91	79.1 (PU)	76.7
Landers	7.3	6/28/92	470.0 (PU)	450
Landers	7.3	6/28/92	534.0 (PF)	552
Parkfield	4.8	10/20/92	9.4 (VC)	9.5
Parkfield	4.8	10/20/92	−7.9 (FR)	−6.6
Parkfield	4.8	10/20/92	6.8 (DL)	8.6
Parkfield	4.8	10/20/92	13.2 (EA)	12.1
Northridge	6.7	1/17/94	21.0 (PU)	20
Northridge	6.7	1/17/94	−5.0 (PF)	−3.2
Parkfield	5.0	12/20/94	120.4 (DL)	114.1
Parkfield	5.0	12/20/94	−21.0 (FR)	−21
Parkfield	5.0	12/20/94	30.0 (EA)	41.8

4. Earthquakes

The coseismic observations can be separated into two parts, the dynamic straingram and the static strain field offset generated by the earthquake. Theory of the strain seismogram can be found in Benioff (1935) and Richards (1976) and will not be pursued further here. The observation of strain offsets from earthquakes has a long history. Early hopes that these offsets could be observed teleseismically (Press, 1965) have not been realized. The primary reason seems to be that tilt and strain observations recorded under conditions of high acceleration in the cracked and fractured near-surface material in tunnels, caves and shallow boreholes, are not reliable because the materials and coupling are not stable (McHugh and Johnston, 1977). Installation of instruments in expansive cement in deep boreholes appears to have solved this problem (Sacks *et al.*, 1971, 1979; McGarr *et al.*, 1982). Data now show that coseismic strain steps can be recorded reliably.

Many examples have been recorded with the network of deep borehole instruments along the San Andreas fault. The best examples are listed in Table 1. For all the events shown here, clear strain offsets have been recorded. An example of the observed strain recorded on the nearest borehole strainmeter (PU) for the $M_W = 6.0$, 1 Oct. 1987, Whittier earthquake is shown in Figure 7a. This, and other similar offsets can be compared with the strain expected at each strainmeter location using the simplest model of each corresponding earthquake. These elastic dislocation models (Press, 1965; Okada, 1985, 1992) assume the moment of the earthquake is generated by uniform slip over a rupture plane that is indicated by the aftershock zone. An example of such a simple dislocation model for the 1987 Whittier earthquake is shown in Figure 7b. In this case the seismically determined moment is 1.4×10^{18} N m, the aftershock zone measures 8 km by 13 km at a depth of 15 km, with a dip of 40° down to the northeast and a strike of N62W. For these dimensions and assuming a shear modulus of 3×10^4 MPa, the slip expected for the earthquake is about 57 cm.

Similar models are routinely generated for the many tens of earthquakes with $M \geq 5.0$ for which we have strain offsets recorded. The calculated and observed offsets for the largest are listed in Table 1 and are plotted in Figure 8. The observed and calculated offsets are in good general agreement except for one example (marked with ?) recorded on the instrument EVSS. Because this instrument was installed just above a large fracture zone, nonlinear effects caused by the accelerations from the seismic waves are more likely to be significant. Thus the total moment release for these earthquakes on the San Andreas fault appears on average to be about 20% larger than that released seismically. Important implications of this general correspondence between observed and calculated strain steps are: (1) that observed strain steps recorded immediately after large earthquakes can be used to make a rapid, albeit preliminary, estimate of the moment of these earthquakes, and (2) crustal response at periods of minutes to hours is still largely elastic.

Postseismic responses observed in these data do not occur unless the earthquake magnitude is greater than $M = 7$, although some effects are sometimes apparent for earthquakes in the $M = 6$–7 range. Most of these effects are due to afterslip,

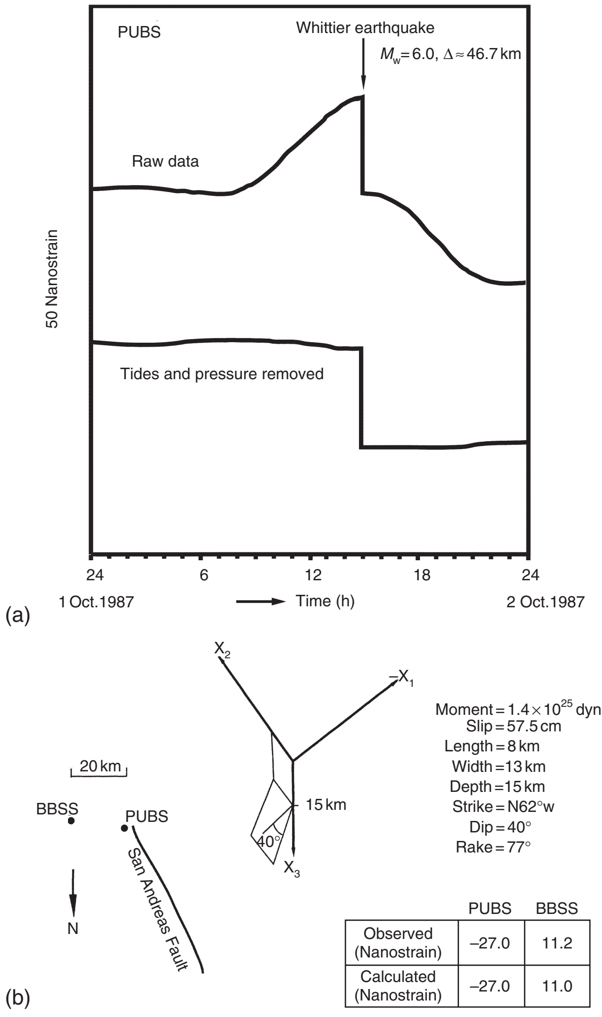

	PUBS	BBSS
Observed (Nanostrain)	−27.0	11.2
Calculated (Nanostrain)	−27.0	11.0

FIGURE 7 (a) Observed strain on 1 Oct. 1987 at PU showing the strain offset generated by the $M_w = 6$ Whittier Narrows earthquake. The variation in the upper plot is due to earth tides. These are predicted and removed in the lower plot. (b) Model of the Whittier Narrows earthquake showing comparison between the observed and predicted strain offsets.

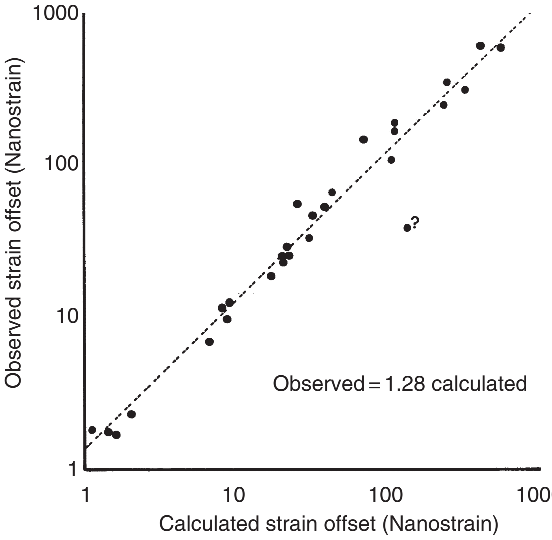

FIGURE 8 Observed coseismic strain offsets as a function of calculated offsets from simple dislocation models of the earthquakes listed in Table 1. See text for comments on point labeled ?.

but other contributions may result from triggered slip on other faults, as suggested by Sacks *et al.* (1979, 1982), to explain postseismic changes following the 1978 Izu, Japan, earthquake. Other short-term and longer-term effects may result from aquifier system response to the incoming seismic waves as observed by Wyatt *et al.* (1994) following the 1992 $M_w = 7.3$ Landers earthquake. In this case the time constant will be determined by the diffusion time constant. Transient strains and tilts related to fluid-diffusion effects triggered by the passage of seismic waves are very evident in measurements taken near the water table (McHugh and Johnston, 1977). The clearest postseismic strain signals have been observed for the larger earthquakes [e.g., Parkfield, 1966 (Smith and Wyss, 1968), Landers, 1992 (Johnston *et al.*, 1994), Loma Prieta, 1989 (Johnston *et al.*, 1990), and Imperial Valley, 1979 (Langbein, *et al.*, 1983)]. These data suggest power law slip in the upper few kilometers with some short-term aquifer re-adjustment effects.

4.1 Slow and Silent Earthquakes

Slow earthquakes refer to fault slip episodes at seismogenic depths that occur with some accompanying seismic radiation in the normal seismic frequency bands. Although long expected to occur (see for example, Kasahara, 1980), little direct evidence for their existence has been found in the few broadband deformation data sets obtained along active faults with enough sensitivity to detect these events. Several different types of slow earthquakes are expected. Slow earthquakes, that precede, and evolve, into "normal" earthquakes have been inferred for the great 1960 Chilean earthquake (Kanamori and Cipar, 1974; Cifuentes and Silver, 1989; Linde and Silver, 1989) and the 1992 $M_w = 7.6$ Nicaragua earthquake (Kanamori and Kikuchi, 1993). Slow earthquakes that follow "normal" earthquakes have been reported following the 1978 $M = 7$ Izu-Oshima earthquake (Sacks *et al.*, 1982), and silent earthquakes with no immediate associated seismicity have been suggested as the cause of strain transients recorded several days before the $M = 7.3$ Japan Sea earthquake (Linde *et al.*, 1988) and with the 1992 event at Sanriku-Oki, Japan (Kawasaki *et al.*, 1995). Large slow earthquakes with related but minor aftershock-like seismicity have occurred on three separate occasions on the San Andreas fault (Linde *et al.*, 1992; Johnston, 1997; Johnston *et al.*, 1998).

Indirect evidence for slow earthquakes has also been proposed on the basis of enhanced tsunami generation (Satake and Kanamori, 1977), anomalous normal modes (Kanamori and Anderson, 1975; Beroza and Jordan, 1990), and anomalous *P* arrivals (Kanamori and Kikuchi, 1993). Overall, when compared to the occurrence rate and moment release of conventional earthquakes, it would be fair to say from the limited near-fault strain data that slow earthquakes are a relatively rare phenomenon on active faults and contribute only in a minor way to total moment release. Nevertheless, they may play an important fundamental role in stress transfer and earthquake triggering (Simpson and Reasenberg, 1994; Harris, 1998).

The most important multiple slow earthquake on the San Andreas fault occurred with about a five-day duration in early December 1992, to the north of San Juan Bautista, California (Linde *et al.*, 1996). Other events were observed in 1996 and 1998. The 1992 sequence was recorded on three near-fault borehole strainmeters and two surface creepmeters along a 10 km section of the fault. The event was accompanied by minor seismicity that was obviously related to the strain data and culminated in surface rupture recorded on a surface creepmeter at the southern end of the strain array. Aseismic moment release for this event totaled about $5\text{–}6 \times 10^{16}$ N m, equivalent to about a $M = 5.1$ earthquake, whereas seismic moment release was more than 100 times less.

Borehole strainmeters at the sites shown in Figure 9a detected large slow coherent strain changes from 10 Dec. to 15 Dec. 1992. The overall event stands out clearly in the

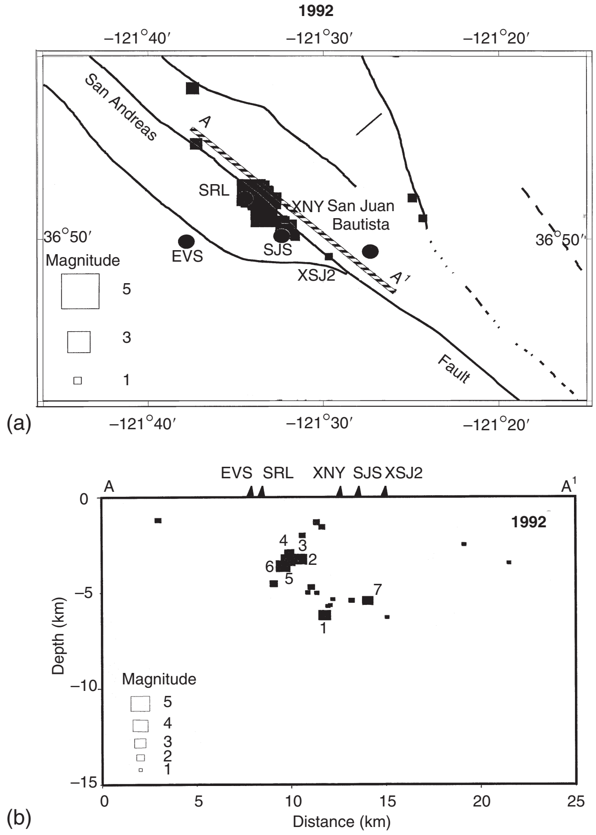

FIGURE 9 (a) Location of borehole dilatational strainmeters EVS, SRL, borehole three-component strainmeters SJS, and creepmeters XSJ2 and XNY with respect to the seismicity (squares) on 11–14 Dec. 1992, associated with a slow earthquake near the town of San Juan Bautista, California (see text). (b) Fault cross-section from A to A′ in (a) showing the locations of earthquakes following the slow earthquake in Dec. 1992, in relation to the position of the strain and creep instruments along the fault.

long-term data as the largest event of this type we have seen on these instruments. A swarm of minor earthquakes (aftershocks?) occurred in this region at the same time. These earthquakes were relocated with a 3D velocity model and their locations are shown on Figure 9a with a symbol size that relates to magnitude and in cross section in Figure 9b. The cross section (indicated by AA′ in Fig. 9b) shows the location of the earthquakes as a function of depth and position relative to the surface instruments. The seismicity outlines a crescent or "donut" shape on the section of fault beneath and between the strainmeters SRL and SJS from a few kilometers to about 8 km deep.

Figure 10a shows the data recorded on the three strainmeters as a function of time. The event began relatively rapidly on 11 Dec. 1992 followed by a slow exponential decay over the next eight days. The long-term decay was interrupted by a series of slow events, labeled A to E, from 11 Dec. to 15 Dec. Some indication of surface creep is evident on XNY following events A, C and E but no surface displacement is evident at XSJ2 until 14 Dec.

A $M = 3.1$ earthquake occurred about two hours before the start of event A and two earthquakes of $M = 3.3$ and 3.2 occurred within the first and third sample interval on both instruments (earthquakes 1, 2, and 3 in the center of Fig. 10a). Two $M = 3.7$ earthquakes (earthquakes 5 and 6) occurred on the next day during event C on both instruments. Smaller earthquakes preceded and followed this event. Coseismic strain changes for all earthquakes are negligible. Because of the instrument sampling intervals, we cannot say with certainty whether these earthquakes preceded or followed the strain events but obviously they are causally related.

Although there are too few observation points to make a robust determination of the source model through formal inversion techniques (Bevington, 1969), we use forward quasi-static modeling to estimate the physical parameters of the simplest physical model that is consistent with the data. Source models are restricted to right-lateral slip segments on the San Andreas fault located in the region of microseismicity and observed surface creep. We search for the simplest quasi-static models that provide consistency with strain amplitudes and duration and surface creep since the strain changes are slow. The best model is shown in Figure 10b and comparison between model predictions (fine lines) and observations (thick lines) are shown on Figure 10a. The model details are generally similar to those given in Linde *et al*. (1996) but it includes three episodes of 3 mm of deeper slip in the region of seismicity, shown in Figure 9b, and slightly different values, shown in Figure 10a, to those used by Linde *et al*. (1996) in the upper section to get a better fit. The event E, coincident with surface creep on XSJ2, is due to surface slip on a patch indicated by W in Figure 10b that has previously failed repeatedly (Gladwin *et al*., 1994). On this patch, slip of 5 mm with rupture velocity of $0.2\,\mathrm{m\,sec^{-1}}$ provides good agreement with data on SJS.

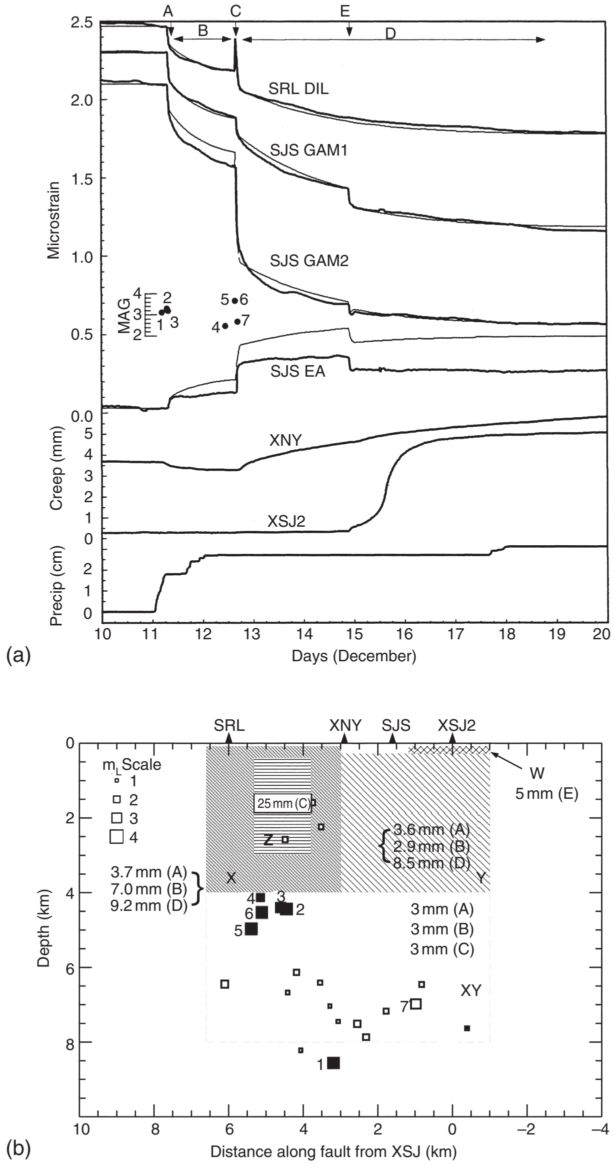

FIGURE 10 (a) Detrended strain data from dilatometers SRL and EVS and tensor strainmeter SJS for the period 10–20 Dec. 1992. Effects from earth tides and atmospheric pressure loading have been predicted and removed from the strain records. The tensor strain data have been converted into fault parallel shear γ_1, NS or EW shear γ_2 and areal strain. Shown also are fault creep data from creepmeter XSJ2 and earthquakes (numbered 1 through 7). Included are comparisons between observed (thin) and calculated (thick) strain-time histories resulting from the simplest model (see text) used to fit the overall strain record and all the slip episodes – subevents A, B, C, D and E discussed in the text. (b) Quasi-static model used to calculate the amplitudes and timescales of the sequence of slow earthquakes beneath San Juan Bautista in Dec. 1992. (See text for description of details.)

Event C has different strain character on SRL than on SJS consistent with changes in the near-surface strain field as the source geometry changes. We have examined all possible model areas between the two instruments and find the only viable solution results from 2.5 cm of slip on a patch Z. The rupture propagates slowly upward with an exponentially decreasing rupture velocity of $0.35\,\mathrm{m\,sec^{-1}}$ resulting in the sign reversal at SRL and the unidirectional changes at SJS.

For the remaining events, strain amplitude ratios cannot be satisfied by uniform slip over a single source area. We require a combination of slip on segments X, Y, and XY shown in Figure 10b. We limit the top of Y to be 0.3 km from the surface for consistency with the lack of creep until 14 Dec. The top of X is 0.1 km deep. We have reasonable control of the extent though the ends could be varied by about 1 km without significantly degrading the fit to the data. Uniform slip that decays with time on X, Y, and XY satisfies the data. This model has slip on X, Y, and XY of 3.7 mm, 3.6 mm, and 3 mm for A, 7.0 mm, 2.9 mm, and 3 mm for B, and 9.2 mm, 8.5 mm, and 3 mm for D (as shown on Fig. 10b) with time constants of 40 min for A, 15 h for B and 43 h for D.

The sequence of events starts with initial slow slip over all XY (event A), followed by slower slip over all XY (event B). Triggered slow upward rupture propagation over Z generates event C, and is followed by continued slow slip over XY (event D) and surface failure recorded on the creepmeter XSJ2 (event E).

The total moment release is $4.5 \times 10^{16}\,\mathrm{N\,m}$. This is approximately equivalent to a $M = 5$ earthquake. In contrast, the seismic moment release was $7 \times 10^{14}\,\mathrm{N\,m}$ (a factor of 76 smaller than the total slow earthquake moment).

The microseismicity that was associated with this sequence occurred in a manner that was clearly related to the near-fault strain. Fitting of a simple exponential relaxation function of the form

$$f(t) = C(1 - \exp^{-at}) \qquad (1)$$

to both the strain data and the cumulative earthquake number indicate similar time constants, $(1/a)$, of about 2.5 days. The occurrence of these slow events, and later events in 1996 and 1998 (Johnston, 1999), has reduced strain energy and has thus reduced (at least temporarily) the likelihood of a large damaging earthquake in this area, in contrast to suggestions by Behr *et al*. (1990).

4.2 Strain Redistribution

Strain redistribution has been clearly observed following each of the largest earthquakes in the San Andreas fault system. The best examples have been obtained for the 1992 Landers earthquake (Wyatt *et al*., 1994; Johnston *et al*., 1994), the 1989 Loma Prieta earthquake (Johnston *et al*., 1990), and the 1987 Whittier earthquake (Linde and Johnston, 1989). Further details of strain redistribution following the Loma Prieta earthquake can be found in Burgmann *et al*. (1997) and Mueller and Johnston (2000).

5. Earthquake Nucleation

As pointed out earlier, laboratory observations and modeling efforts suggest that fault failure occurs when displacements exceed those for peak shear stress. Increased deformational "weakening" occurs before the dynamic slip instability that results in an earthquake. In rock mechanics terminology this is called "tertiary creep" (Jaeger and Cook, 1976). In terms of laboratory-determined rate or state-dependent friction (Ruina, 1983; Dieterich, 1994), it is called "slip weakening." That nonlinear strain precedes rupture has provided hope that detection of these strain changes will lead to a method for earthquake prediction. At issue is the scale on which this occurs. Since continuous strain measurements near moderate to large earthquakes thus far have failed to detect any indications of exponentially increasing strain (Johnston *et al*., 1990, 1994; Wyatt, 1994; Abercrombie *et al*., 1995), the scale must be small compared to the eventual rupture size. Here we discuss just how small this might be.

5.1 Field Observations

We choose just one typical example of short-term and intermediate-term strain obtained before, and immediately above, a moderate magnitude earthquake to illustrate this scale. The event we choose was one of three $M = 5$ earthquakes that occurred beneath the Parkfield strainmeter array shown in Figure 11a. A cross section of these events is shown in Figure 11b. The first was a $M = 4.7$ earthquake that occurred on 31 Oct. 1992. The second was a $M = 4.8$ earthquake that occurred on 20 Nov. 93 and the third was a $M = 5$ earthquake on 24 Dec. 1994.

Figure 12a shows the strain data from FRS and DLS for the $M = 5$ event on 20 Dec. 94 for the five days before and after this earthquake. The vertical scale is in 10 nanostrain units in the upper plot that shows the strain offsets (+31 nanostrain at FR and − 94 nanostrain at DL) generated by the earthquake. The scale is expanded in the lower plot by a factor of 50 (0.5 nanostrain units).

Figure 12b (upper) shows the strain seismograms for this earthquake recorded on these two instruments. The expanded timescale in the lower plot shows the data for these events in the last seconds before rupture. Here the vertical scale is 1000 nanostrain. Figure 12c shows the strain vertical scale expanded by 100 in the upper plot (units of 10 nanostrain) and by 10 000 in the lower plot (units of 100 picostrain). The occurrence time of the earthquake is shown with an arrow. Strain changes, if they occurred before the event, appear to be less than 0.01 nanostrain. Similar observations were obtained for the other two $M = 5$ earthquakes.

It is apparent for these events, and for the 17 or so moderate to large earthquakes for which we have near-field strain data, that none of the strain records shows any indication of accelerating strain prior to rupture at our ability to resolve

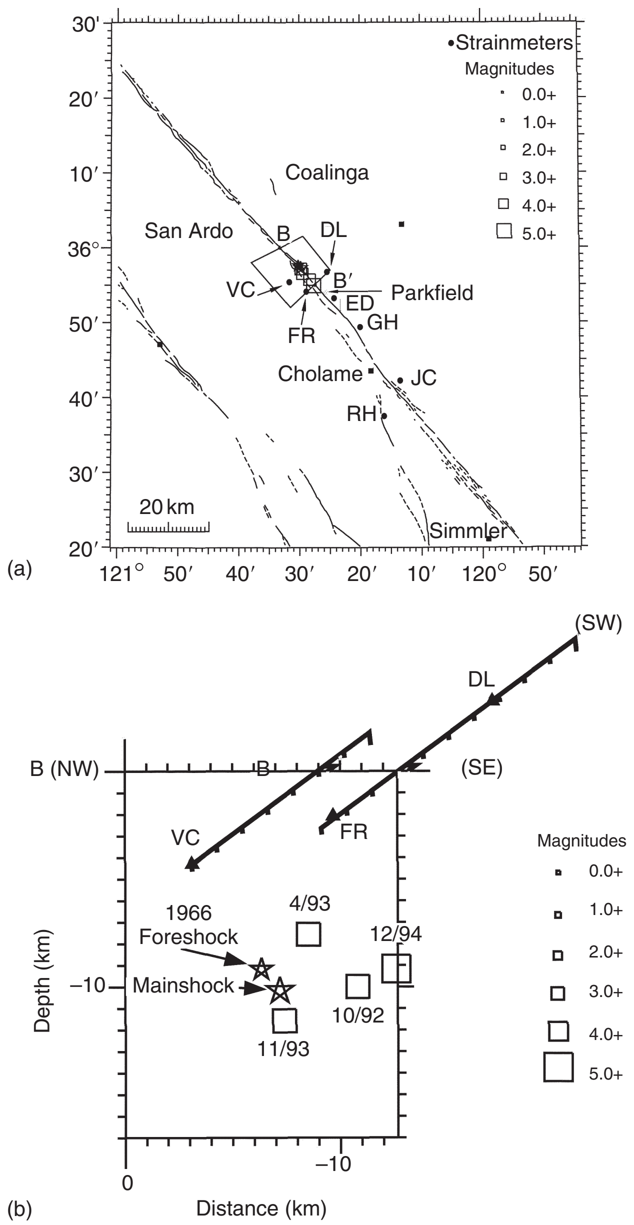

FIGURE 11 (a) Map of Parkfield showing the location of three near-magnitude 5 earthquakes beneath the dilatational strainmeters VC, FR, and DL on 20 Oct. 1992, 14 Nov. 1993, and 20 Dec. 1994. The locations of the various events are shown in cross section in (b). (b) Seismicity cross section showing the location of three near-magnitude 5 earthquakes beneath the dilatational strainmeters VC, FR, and DL on 20 Oct. 1992, 14 Nov. 1993, and 20 Dec. 1994. Also shown is the hypocenter of the 1966 Parkfield mainshock (Star).

strain (0.01 nanostrain over seconds and 1.0 nanostrain over days). This does not mean that accelerating strain is not occurring, only that it is below our measurement resolution. Another way of saying this is that the maximum possible preseismic slip moment in the eventual hypocenter produces strains at the instrument that are less than, or equal to our measurement resolution.

The maximum possible precursive slip moment expressed as a percentage of coseismic moment is plotted against seismic moment for these earthquakes in Figure 13. In general, moment release before these earthquakes is less than a few percent and perhaps less than 0.1% if we take the later data for which the signal-to-noise is best (Johnston *et al*., 1990, 1994; Wyatt, 1994). What this most likely means is that rocks do indeed fail as expected but that the initial slip is small and localized compared to the final or total slip. The ratio of total slip to nucleation slip is thus large and rupture initiation is inhomogeneous in agreement with a variety of theoretical and seismological observations (discussed below).

Since our ability to resolve strain changes improves at shorter periods, we can place better constraints on the largest precursive slip moment that might occur as a function of decreasing period or increasing resolution. At periods of seconds we can resolve 0.01 nanostrain, over hours it is 0.1 nanostrain and over weeks it is 1.0 nanostrain. Simple elastic dislocation calculations (Okada, 1985, 1992) allow us to calculate strains at these different levels for precursive slip moments at various depths. For example, a slip moment of 10^{12} N m at a depth of 5 km will produce surface strains of 0.01 nanostrain. If the depth is 8 km, the slip moment would be 3×10^{12} N m. Precursive slip moment as a function of resolution (or period) and depth is shown in Figure 14a.

How big might the nucleation zone be? Let us assume displacement, U, is proportional to rupture length, L. Observation and theory (constant stress drop assumption) support this assumption for earthquakes with M_{L} less than 6 (e.g., see Scholz, 1997). Then,

$$U = KL\Delta\sigma \tag{2}$$

where $K \approx 10^{-7}\,\mathrm{m\,MPa^{-1}\,km^{-1}}$, L = rupture dimension, and $\Delta\sigma$ = stress drop ($\approx$1 MPa). Therefore, the moment M is given by:

$$M \approx \mu 10^{-4} L^3 \tag{3}$$

where μ is the rigidity. It is thus possible to obtain crude limits on the nucleation size since we have limits on the maximum precursory slip moment that can be released over periods of weeks to seconds before seismic rupture. Figure 14b shows the equivalent limit on the source zone size obtained from Eq. (3) as a function of resolution (or period) and depth. For the $M = 5$ earthquakes at Parkfield, where we are within 7 km of the source, the maximum size of the nucleation patch in the last few seconds before seismic radiation occurs, is about 69 m. At longer periods, where the resolution is less, the constraint on size becomes poorer. On time periods of several weeks where our capability to resolve strain changes is not more than a few nanostrain, we cannot resolve nucleation regions unless their dimensions are greater than several hundred meters. However, it is important to note that, in the last hours to seconds before rupture, we would expect the largest nonlinear strain

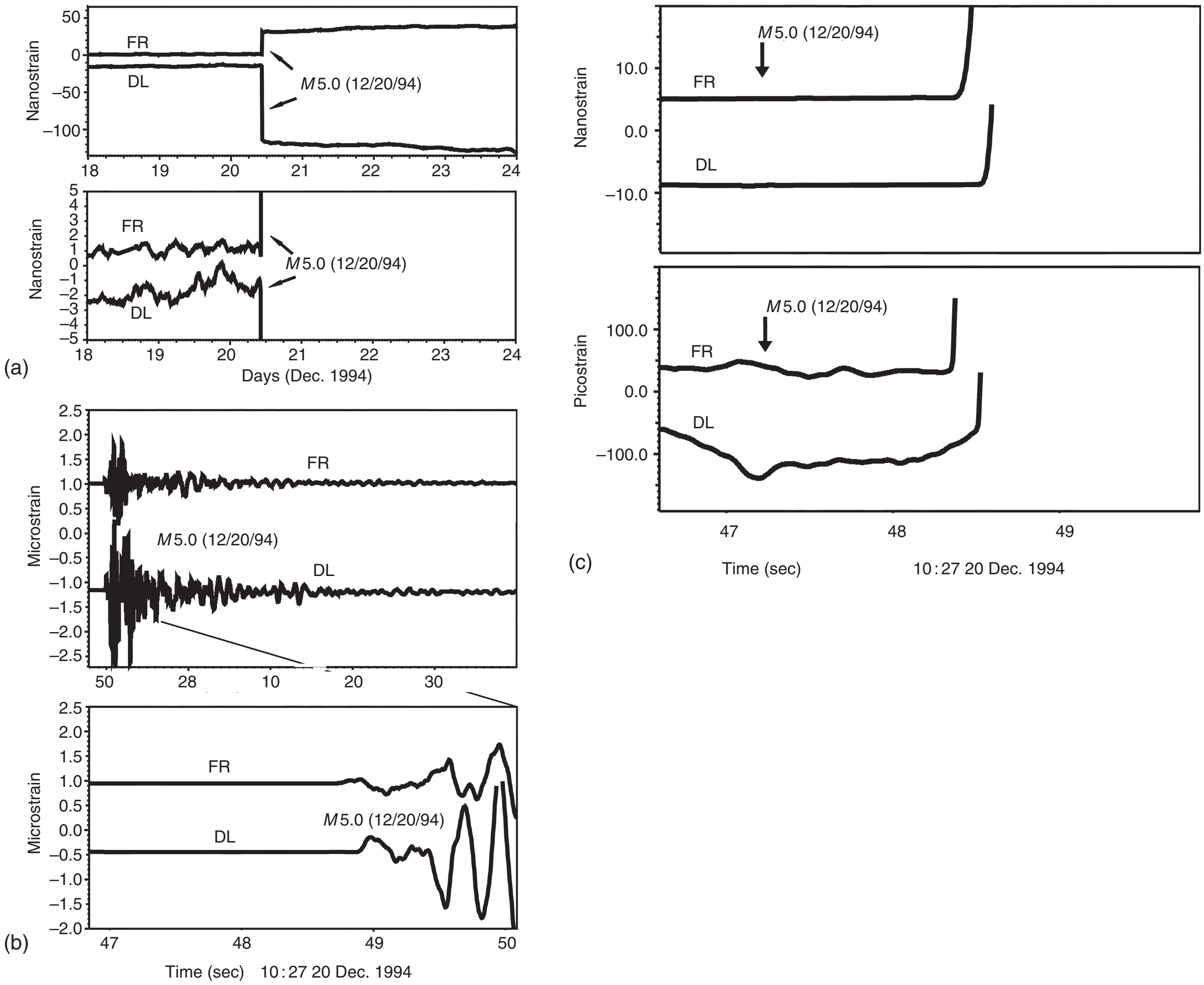

FIGURE 12 (a) Strain time histories from strainmeters FR and DL on opposite sides of the San Andreas fault from 15 to 26 Dec. 1994. Full-scale on the upper plot is 200 nanostrain that on the lower plot is 10 nanostrain. (b) Expanded time-history at 10 : 27 UT on 20 Dec. 1994. The upper plot shows the strain seismogram of the $M = 5.0$ earthquake starting at about 10 : 27 : 49 UT. The lower plot shows an even more expended section during the 2 sec before the first arrival. The strain units on the vertical scale are 1000 nanostrain. (c) Expanded vertical scale for the time-history at 10 : 27 UT on 20 Dec. 1994 shown in (b) (lower). The upper plot shows the vertical scale expanded by 100 and the lower plot shows the scale expanded by 10 000. The actual occurrence time is shown with a vertical arrow. Similar data were obtained for the other two $M = 5$ earthquakes on these instruments.

(as indicated in Fig. 1). It is during this time period that strain resolution is the best. The fact that no clear indication of accelerating strain is apparent in any of the strain records suggests nucleation patch sizes of perhaps a few tens of meters. Repeating microearthquakes on patches with this dimension have been observed by Nadeau and McEvilly (1997).

These data similarly constrain changes in pore pressure in the fault zone that may be related to the failure process. If we assume no hydraulic connectivity between a region of high pore pressure on the fault zone (such as proposed by Byerlee, 1990, 1993) and ignore for the moment how pore pressure changes in these regions might occur, it is obvious from simple calculations of strain generated by changes in pore pressure for regions with dimensions of a few hundred meters and depths of about 5 km that rapid changes in pore pressure of 0.1 MPa should be readily detected, though not necessarily recognized as such. If hydraulic communication with the surroundings does exist, smaller pore pressure changes might be detected as poroelastic strain as fluids diffuse out to greater distances, in effect increasing the source size. Small changes

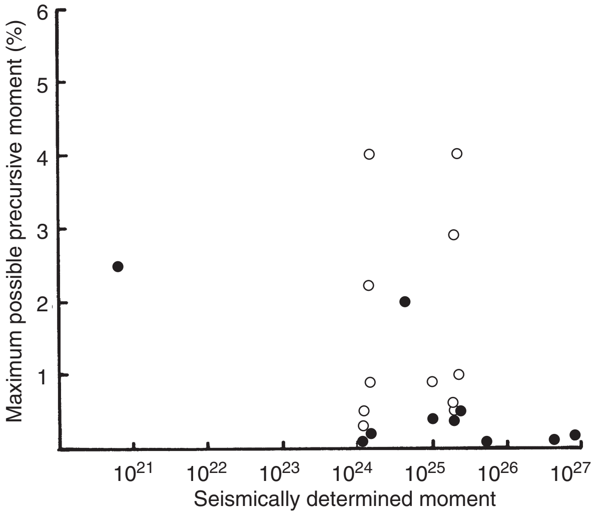

FIGURE 13 Plot of maximum possible prerupture moment as a percentage of the seismically determined moment for the events studied listed in Table 1. Closed circles show data obtained within one rupture length of subsequent earthquakes. Open circles show data obtained at greater distances.

in the local geometry of regions with high pore pressure such as, for example, a 100 m by 100 m zone at 5 km depth dropping pressure by doubling its size probably would not be detectable.

It is also apparent in these data that large-scale changes in elastic properties within the fault zone are not occurring near these instruments. If they were, we would expect changes in tidal shear strain and volumetric strain response. Observations of earthtide response before and after the largest earthquakes (Landers, Loma Prieta, etc.) indicate that if measurable changes occur, they are less than 1% (Linde *et al.*, 1992).

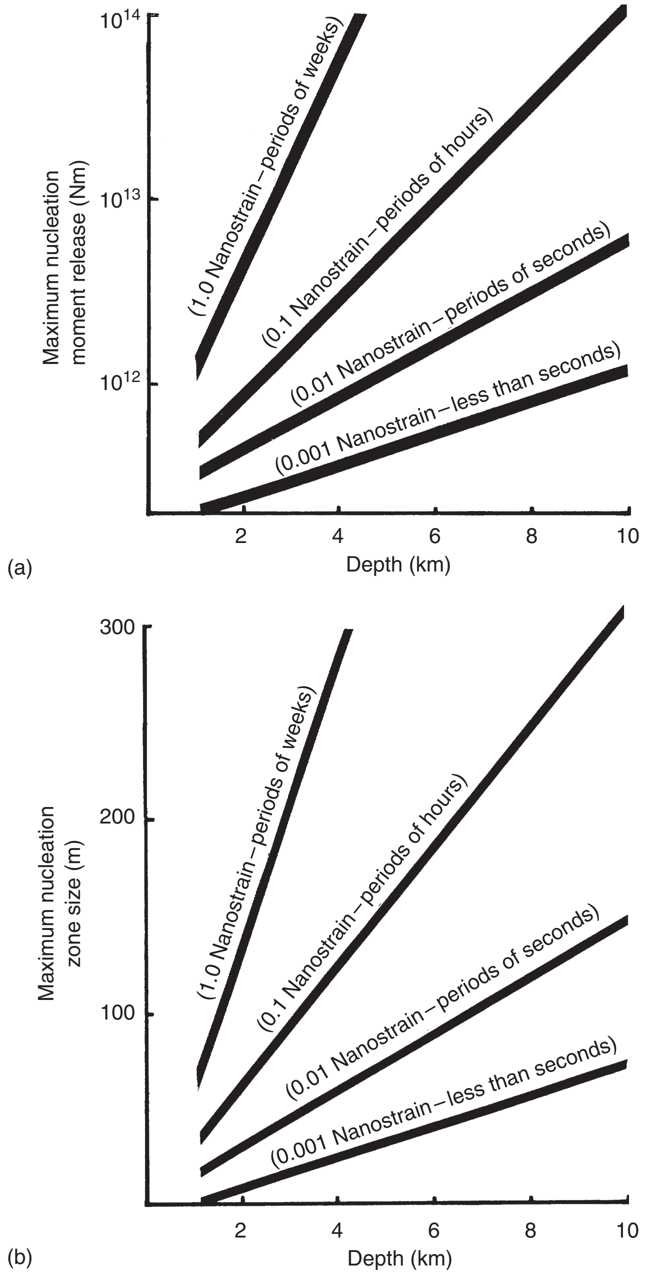

FIGURE 14 (a) Maximum nucleation moment release allowable as a function of nucleation source depth for strainmeter resolution in nanostrain at different periods. Over periods of seconds the resolution is 0.01 nanostrain, over periods of hours it is 0.1 nanostrain and over periods of weeks it is 1 nanostrain. (b) Maximum nucleation zone size allowable as a function of nucleation source depth for strainmeter resolution in nanostrain at different periods. Over periods of seconds the resolution is 0.01 nanostrain, over periods of hours it is 0.1 nanostrain and over periods of weeks it is 1 nanostrain.

5.2 Comparison with Laboratory Observations

It seems unlikely that both the wealth of laboratory data describing anelastic deformation of unfractured crustal rocks before failure and theoretical calculations of anelastic deformation during crack initiation and crack behavior are not relevant to initiation of fault failure. However, it is clear from existing surface and borehole strain data that slip instability over the entire subsequent fault rupture is not possible unless the time constant for rupture initiation is unrealistically short or prerupture deformation is exceedingly small. Laboratory measurements of crustal rocks under high confining pressure indicate anelastic strains before failure are comparable to the elastic strain release upon failure (Jaeger and Cook, 1976). On the other hand, frictional slip on preexisting slip surfaces in large-scale laboratory friction experiments (Dieterich, 1981) indicates nucleation slip does initiate within a small nucleation region. Dieterich (1992) shows numerical calculations that indicate the size of these regions should be 1–10 m for both smooth or rough initial stress distributions, consistent with the upper bounds allowed by the strain data. It would appear from both data that the scale on which rupture initiates is several orders of magnitude smaller than that of the subsequent earthquake. If so, the fault model relevant to this process must be inhomogeneous in character to accommodate these observations that crustal failure does not occur simultaneously across the entire rupture zone, but is apparently triggered by failure of small localized zones.

Comparisons can also be made to the duration of nucleation derived by Dieterich (1994), who determined an expression for the time to failure during nucleation as a simple function of sliding velocity. For reasonable values of stiffness, velocity, normal stress gradient, etc., the duration of nucleation is on the order of 1–10 sec. This is in general agreement with the indications from the strain data. Furthermore, the nucleation moment from these laboratory measurements (Dieterich, 1992) is also only a small fraction of the slip moment as seen in the strain data.

5.3 Comparison with Current Theory

That an inhomogeneous faulting model may best describe the initiation of failure is not at all surprising. Wyss and Brune (1967) and many researchers since then have made similar suggestions. Based on careful analysis of seismic waveforms and on synthetic waveform generation, Kanamori (1981) and Lay *et al*. (1982) have shown that an inhomogeneous rupturing model is required to explain the complex waveforms generated by many large earthquakes. These data have been used to suggest that regions of greater strength (barriers or asperities) can be broken during fault failure and energy release from these regions contributes to the seismic radiation.

Inhomogeneous fault models have been proposed by McGarr (1981) to explain peak ground motion in an earthquake, by Dieterich (1986) to explain simulated faulting in laboratory samples, and, in a more general way, by Rundle *et al*. (1984) to explain seismicity gaps, fault roughness indicated by complex seismic waveforms, and apparent triggering effects. The data reported here are consistent with the suggestion outlined above that rupture initiation most likely occurs at smaller regions of higher strength which, when broken, allow runaway catastrophic failure. An inhomogeneous failure model, in which various areas of the fault plane have different stress-slip constitutive laws, appears necessary to explain both the processes that lead to failure and those that occur following failure. This type of model was proposed by Rundle *et al*. (1984). Other inhomogeneous failure models are also possible.

6. Conclusions

Observations of crustal strain at high sensitivity near active faults allow us to identify the main features of strain transients that occur. On timescales of years, the primary features are uniform strain accumulation with occasional strain steps generated by large earthquakes, followed sometimes by post-seismic strain redistribution (Savage, 1983; Burgmann *et al*., 1997). Conventional geodetic, EDM instruments and GPS instruments are best used to obtain these data. At shorter timescales (months to milliseconds), higher strain resolution is possible either by spatial averaging with a laser interferometer over about 500 m to suppress surface noise (Wyatt, 1988), or by installing instruments at depth in boreholes (Sacks *et al*., 1971; Gladwin, 1984).

Strain transients associated with fault creep events indicate that these events result primarily from near-surface soil failure that is driven by deeper smoother fault slip. These events can sometimes be triggered by high accelerations during the passage of seismic waves from large nearby earthquakes (Simpson *et al*., 1988) and sometimes by rainfall (Schulz *et al*., 1982). In either case the event-like character is not of much interest in fault mechanics. However, the net creep-time history does appear to reflect the net slip on the fault and long-term changes in fault creep rate are important indicators of change in fault slip rate at depth.

There is little evidence of slip waves propagating slowly along active faults, at least on timescales of months to minutes. Either the amplitudes of these slip waves, if they exist, is very small ($\leq$1 cm), or the period is so large that they cannot be resolved from the longer-term noise. Even at long periods (month to years), evidence of slip waves is not apparent in 2-color EDM data at Parkfield and San Juan Bautista where periodic surface displacements on opposite sides of the San Andreas fault of a millimeter or so should be readily detectable. The resolution of the 2-color EDM is about 0.1 mm (Langbein, 1981).

Coseismic strain offsets recorded on borehole strainmeters for earthquakes with magnitudes from 3 to 7 are generally in good agreement with offsets expected from simple dislocation models of these earthquakes. This suggests that the use of dislocation models for calculating coseismic stress changes (e.g., Reasenberg and Simpson, 1992) is generally valid, or at least far removed from the rupture ends. The variable and general amplified coseismic offset response to earthquakes previously observed in the cracked and fractured material near the Earth's surface, and in caves or tunnels, appears to be avoided by installing instruments in grout in deep boreholes. An important implication of these observations is that strain redistribution from an earthquake is transmitted largely elastically through the complex geology and fault geometry in these regions. A second important implication is that preliminary moment determinations can be made within a few tens of minutes of the occurrence of moderate magnitude earthquakes from observation of the strain offsets generated by these earthquakes.

Unambiguous strain recordings on several borehole strainmeters now exist of several slow earthquakes on the

San Andreas fault near San Juan Bautista and other locations. The clearest event occurred on a 6 km long by 8 km wide segment of the fault just to the north of San Juan Bautista during a 4-day period starting on 11 Dec. 1992. This event is complex with a number of episodes. Evidence exists for both slip acceleration and variable slip geometry for these episodes. This event and later events in 1996 and 1998 are unique in the 15-year record of strain at these sites. The 1992 event generated shear-strains exceeding 1 microstrain on the tensor strainmeter MSJS near the town of San Juan Bautista and dilatational strain exceeding 0.7 microstrain at the dilatational strainmeter SRLS 5 km to the northwest along the fault. A third dilatometer installed some 7 km from the fault recorded strains of about 0.1 microstrain. Quasi-static modeling of this event indicates that it probably ruptured a 50 km^2 segment of the fault in less than 10 min and that episodes of exponential-like slip, either triggered or accelerated by the larger aftershocks, continued with time. Nearly four days after the event started at depth, it reached the surface and generated a 3-day episode of surface fault displacement that was recorded on a surface creepmeter XSJ2 east of the town of San Juan Bautista. The entire sequence generated event moment release that was equivalent to a $M = 5$ earthquake.

Actual recordings of slow earthquakes have been rarely reported in the geophysical literature. The question naturally arises as to whether this is because they are truly rare, or whether the situation has resulted from the paucity of high-sensitivity strain instruments installed near active faults and the relatively short history of high-quality recordings. In any case, as a consequence of these slow earthquakes near San Juan Bautista, the immediate likelihood of moderate magnitude earthquakes in this region has been reduced, in contrast to suggestions by Behr *et al*. (1990).

Popular views of the Earthquake nucleation process and fault kinematics have included suggestions of nonlinear deformation prior to rupture in regional-scale “preparation zones” of earthquakes (Rice and Rudnicki, 1979), strain redistribution by “crustal block interaction” (Jackson and Molnar, 1990), propagating aseismic slip waves (Kasahara, 1979), and variation in the material properties of near-fault materials with time and location (Dobrovolsky *et al*., 1979).

In contrast, attempts to detect preseismic strain change near several recent moderate earthquakes during the final hours to seconds approaching rupture near many moderate earthquakes in California and Japan have failed. This places important constraints on possible moments and dimensions of nucleation events. First, since short-term nonlinear precursive strains greater than a nanostrain have not been observed in the eventual epicentral region prior to rupture, moment release during nucleation is thus ≈ 300 times smaller than that released statically and $\approx 10\,000$ times smaller than that released dynamically. For the best cases investigated, the greatest possible preseismic moment is less than 0.1% of the final seismic or geodetic moment. This implies tertiary creep prior to rupture is minimal over the entire eventual rupture zone, as expected for brittle failure.

Secondly, the dimensions of the rupture nucleation region for the largest earthquakes for which we have high-resolution near-field preseismic strain data, are less than several tens of meters. This is consistent with nucleation dimensions suggested by clusters of repeating microseismicity (Nadeau and McEvilly, 1997) and with indications from earthtidal response that fault zone material properties are invariant on timescales of days to months (Linde *et al*., 1992).

The apparent small size of the rupture initiation moments compared to the total earthquake moments suggests that there is no scaling of the nucleation process with earthquake magnitude. This is inconsistent with suggestions by Ellsworth and Beroza (1995) and Iio (1995) that nucleation scales with earthquake magnitude. In fact, one of the earthquakes used by Ellsworth and Beroza (1995) to demonstrate nucleation is the one shown in Figure 12. The strain data require no processing, have a flat response from 50 Hz to DC and show no indication of nucleation prior to the first seismic wave arrival. The basic failure process thus apparently involves rupture nucleation and runaway. High pore pressure fluids may be associated with this process but if pore pressure changes drive the nucleation process, these changes are less than about 0.1 MPa at seismogenic depths.

An inhomogeneous faulting model for which different areas of the fault plane have either different constitutive properties or different stress-slip constitutive laws most easily explain these data. This type of model was proposed by Rundle *et al*. (1984) and is indicated by observations of complex seismic waveform generation during rupture (Kanamori, 1981; Lay *et al*., 1982). For these inhomogeneous models, failure initiation occurs in relatively localized zones and expands until barriers of sufficient strength to stop the rupture, are encountered. The processes that lead to failure as well as those that follow failure are inhomogeneous in character. Energy driving the system appears to come from uniformly accumulated elastic strain energy (Prescott *et al*., 1979). Detection of rupture nucleation apparently will require these highly sensitive and stable instruments be installed even closer than at present to the hypocenters of large earthquakes.

A variety of postseismic responses have been observed. This mostly reflects continuing slip following large earthquakes, with contributions in some cases from the equilibration of the fluid regime. During this postseismic period, slip varies as log (time) consistent with either relaxation of a near-surface region after stress-induced velocity strengthening (Scholz, 1990), or a fluid-diffusion process. Afterslip is common in regions where aseismic fault slip occurs, such as on the San Andreas fault following the 1966 Parkfield earthquake (Smith and Wyss, 1968), and on the Imperial fault following the 1979 Imperial Valley earthquake (Langbein *et al*., 1983).

Acknowledgments

Numerous colleagues have provided stimulating discussions. We thank Bob Mueller and Doug Myren for help with installation and maintenance of the strain instruments and John Langbein for contributions to Figure 2. Ruth Harris and Nick Beeler provided thoughtful reviews.

References

Abercrombie, R.E., *et al.* (1995). *Bull. Seismol. Soc. Am.* **85**, 1873–1879.
Agnew, D.C. (1997). *J. Geophys. Res.* **102**, 5109–5110.
Andrews, D.J. (1976). *J. Geophys. Res.* **81**, 5679–5687.
Atkinson, B.K. (1979). *Pure Appl. Geophys.* **117**, 1011–1024.
Behr, J., *et al.* (1990). *Trans. Am. Geophys. Un.* **71**, pp. 1645.
Benioff, H. (1935). *Bull. Seismol. Soc. Am.* **25**, 283–309.
Beroza, G. and T. Jordan (1990). *Seismol. Res. Lett.* **61**, pp. 27.
Bock, Y. (1997). *Trans. Am. Geophys. Un.* **78**, F165.
Brune, J.N. (1979). *J. Geophys. Res.* **84**, 2195–2198.
Bevington, P.R. (1969). "Data Reduction and Error Analysis for the Physical Sciences", McGraw Hill.
Burgmann, R., *et al.* (1997). *J. Geophys. Res.* **102**, 4933–4955.
Byerlee, J. (1990). *Geophys Res. Lett.* **17**, 2109–2112.
Byerlee, J. (1993). *Geology* **21**, 303–306.
Cifuentes, I.L. and P.G. Silver (1989). *J. Geophys. Res.* **94**, 643–663.
Das, S. and C.H. Scholz (1981). *J. Geophys. Res.* **86**, 6039–6051.
Dieterich, J.H. (1979). *J. Geophys. Res.* **84**, 2161–2168.
Dieterich, J.H. (1981). *AGU Geophys. Monogr. Ser.* **24**, 103–120.
Dieterich, J.H. (1986). *AGU Geophys. Monogr.* **37**, 37–47.
Dieterich, J.H. (1992). *Tectonophysics.* **211**, 115–134.
Dieterich, J.H. (1994). *J. Geophys. Res.* **99**, 2601–2618.
Dobrovolsky, I.P., *et al.* (1979). *Pageoph* **117**, 1025–1044.
Eaton, J.P. (1985). *US Geol. Surv. Open File Report 85–44*, 44–60.
Ellsworth, W.L. and G.C. Beroza (1995). *Science* **268**, 851–855.
Evans, K.F., *et al.* (1981). *J. Geophys. Res.* **86**, 3721–3735.
Freund, L.B. (1979). *J. Geophys. Res.* **84**, 2199–2209.
Gladwin, M.T. (1984). *Rev. Sci. Instrum.* **55**, 2011–2016.
Gladwin, M.T., *et al.* (1987). *J. Geophys. Res.* **92**, 7981–7988.
Gladwin, M.T., *et al.* (1991). *Geophys. Res. Lett.* **18**, 1377–1380.
Gladwin, M.T., *et al.* (1994). *J. Geophys. Res.* **99**, 4559–4565.
Goulty, N.R. and R. Gilman (1978). *J. Geophys. Res.* **83**, 5415–5419.
Harris, R.A. (1998). *J. Geophys. Res.* **103**, 24347–24358.
Harrison J.C. (1976). *J. Geophys. Res.* **81**, 319–328.
Hart, R.H.G., *et al.* (1996). *J. Geophys. Res.* **101**, 25553–25571.
Heaton, T.H. (1982). *Bull. Seismol. Soc. Am.* **72**, 2181–2200.
Iio, Y. (1995). *J. Geophys. Res.* **100**, 15333–15349.
Ito, T.H. (1982). *Bull. Seismol. Soc. Am.* **20**, 2181–2200.
Jackson, J. and P. Molnar (1990). *J. Geophys. Res.* **95**, 22073–22087.
Jaeger, J.C. and N.G.W. Cook (1976). "Fundamentals of Rock Mechanics," Chapman and Hall.
Johnston, M.J.S. (1997). *Trans. Am. Geophys. Un.* **79**, F156.
Johnston, M.J.S. (1999). *Trans. Am. Geophys. Un.* **80**, F691.
Johnston, M.J.S. and R.D. Borcherdt (1984). *Trans. Am. Geophys. Un.* **65**, 1015.
Johnston, M.J.S., *et al.* (1976). *Nature* **260**, 691–693.
Johnston, M.J.S., *et al.* (1977). *J. Geophys. Res.* **82**, 5683–5691.
Johnston, M.J.S., *et al.* (1986). *J. Geophys. Res.* **91**, 11497–11502.
Johnston, M.J.S., *et al.* (1987). *Tectonophysics* **144**, 189–206.
Johnston, M.J.S., *et al.* (1990). *Geophys. Res. Lett.* **17**, 1777–1780.
Johnston, M.J.S., *et al.* (1994). *Bull. Seismol. Soc. Am.* **84**, 799–805.
Johnston, M.J.S., *et al.* (1998). *Trans. Am. Geophys. Un.* **79**, F600.
Kanamori, H. (1981). *Maurice Ewing Series IV*, pp. 1–19 *American Geophysics Union*.
Kanamori, H. and D.L. Anderson (1975). *J. Geophys. Res.* **80**, 1075–1078.
Kanamori, H. and J. Cipar (1974). *Phys. Earth Planet. Inter.* **9**, 128–136.
Kanamori, H. and M. Kikuchi (1993). *Nature* **361**, 714–716.
Kasahara, K. (1979). *Tectonophysics* **52**, 329–341.
Kasahara, K. (1980). "Earthquake Mechanics," Cambridge University Press.
Kasahara, M., *et al.* (1983). *Tectonophysics* **97**, 327–336.
Kawasaki, I., *et al.* (1995). *J. Phys. Earth* **43**, 105–116.
Kostrov, B.V. (1966). *J. Appl. Math. Mech.* **30**, 1241–1248.
Langbein, J.O. (1981). *J. Geophys. Res.* **62**, 4941–4948.
Langbein, J.O. and H. Johnson (1996). *J. Geophys. Res.* **102**, 591–604.
Langbein, J., *et al.* (1983). *Bull. Seismol. Soc. Am.* **73**, 1203–1224.
Lay, T., *et al.* (1982). *Earthqu. Predict. Res.* **1**, 3–71.
Linde, A.T. and M.J.S. Johnston (1989). *J. Geophys. Res.* **94**, 9633–9643.
Linde, A.T. and P.G. Silver (1989). *Geophys. Res. Lett.* **16**, 1305–1308.
Linde, A.T., *et al.* (1988). *Nature* **334**, 513–515.
Linde, A.T., *et al.* (1992). *Geophys. Res. Lett.* **19**, 317–320.
Linde, A.T., *et al.* (1993). *Nature* **365**, 737–740.
Linde, A.T., *et al.* (1996). *Nature* **383**, 65–68.
Lorenzetti, E. and T.E. Tullis (1989). *J. Geophys. Res.* **94**, 12343–12361.
Matsu'ura, M. and T. Tanimoto (1980). *J. Phys. Earth* **28**, 103–118.
Marone, C.J., *et al.* (1991). *J. Geophys. Res.* **96**, 8441–8452.
McGarr, A. (1981). *J. Geophys. Res.* **86**, 3901–3912.
McGarr, A., *et al.* (1982). *Geophys. J. R. Astron. Soc.* **70**, 717–740.
McHugh, S. and M.J.S. Johnston (1977). *J. Geophys. Res.* **82**, 5692–5697.
McHugh, S. and M.J.S. Johnston (1978). *Bull. Seismol. Soc. Am.* **68**, 155–168.
McHugh, S. and M.J.S. Johnston (1979). *Proc. Eur. Geophys. Soc.*, 181–201.
McTigue, D.F. and P. Segall (1988). *Geophys. Res. Lett.* **15**, 601–604.
Miller, S.A., *et al.* (1999). *J. Geophys. Res.* **104**, 10621–10638.
Mjachkin, V.I., *et al.* (1975). *Pageoph* **113**, 169–181.
Mogi, K. (1981). *J. Soc. Mater. Sci. Jpn.* **30**, 105–118.
Mogi, K. (1985). "Earthquake Prediction." Academic Press.
Mogi, K., *et al.* (1982). *Abstr. Seismol. Soc. Jpn.* No. 1, 128.
Mueller, R.J. and M.J.S. Johnston (2000). *US Geol. Surv. Open File Report 00–146*.
Nadeau, R.M. and T.V. McEvilly (1997). *Bull. Seismol. Soc. Am.* **87**, 1463–1472.
Okada, Y. (1985). *Bull. Seismol. Soc. Am.* **75**, 1135–1154.
Okada, Y. (1992). *Bull. Seismol. Soc. Am.* **82**, 1018–1040.
Pollitz, F., *et al.* (1998). *Science* **103**, 1245–1249.

Prescott, W.H., *et al.* (1979). *J. Geophys. Res.* **84**, 5423–5435.

Press, F. (1965). *J. Geophys. Res.* **70**, 2395–2412.

Press, F. and C. Allen (1995). *J. Geophys. Res.* **100**, 6421–6430.

Rabbel, W. and J. Zschau (1985). *J. Geophys.* **56**, 1–99.

Reasenberg, P.A. and R.W. Simpson (1992). *Science.* **255**, 1687–1690.

Rice, J.R. (1983). *Pure Appl. Geophys.* **121**, 443–475.

Rice, J.R. and J.W. Rudnicki (1979). *J. Geophys. Res.* **84**, 2177–2193.

Rice, J.R. (1992). In: "Earthquake Mechanics and Transport Properties of Rocks", pp. 475–503, Academic Press.

Richards, P.G. (1976). *Bull. Seismol. Soc. Am.* **65**, 93–112.

Rikitake, T. (1976). "Earthquake Prediction," Elsevier.

Ruina, A. (1983). *J. Geophys. Res.* **88**, 10359–10370.

Rundle, J.B., *et al.* (1984). *J. Geophys. Res.* **89**, 10219–10231.

Sacks, I.S., *et al.* (1971). *Papers Meteorol. Geophys.* **22**, 195–207.

Sacks, I.S., *et al.* (1978). *Nature* **275**, 599–602.

Sacks, I.S., *et al.* (1979). *Maurice Ewing Series IV*, pp. 617–628, American Geophysics Union.

Sacks, I.S., *et al.* (1982). *Tectonophysics* **81**, 311–318.

Sadovsky, M.A., *et al.* (1972). *Tectonophysics* **14**, 295–307.

Satake, K. and H. Kanamori (1977). *J. Geophys. Res.* **82**, 5692–5697.

Savage, J.C. (1971). *J. Geophys. Res.* **76**, 1954–1966.

Savage, J.C. (1983). *Annu. Rev. Earth. Planet. Sci.* **11**, 11–43.

Scholz, C.H. (1990). "Mechanics of Earthquakes and Faulting," Cambridge University Press, New York.

Scholz, C.H. (1997). *Bull. Seismol. Soc. Am.* **87**, 1074–1077.

Schulz, S.S., *et al.* (1982). *J. Geophys. Res.* **87**, 6977–6982.

Segall, P. and J.R. Rice (1995). *J. Geophys. Res.* **100**, 22155–22171.

Shaw, B.E. (1997). *J. Geophys. Res.* **102**, 27367–27377.

Silverman, S., *et al.* (1989). *Bull. Seismol. Soc. Am.* **79**, 189–198.

Simpson, R.W. and P. Reasenberg (1994). *US Geol. Surv. Prof. Pap.* **1550-F**, 55–89.

Simpson, R.W., *et al.* (1988). *Pageoph* **126**, 665–685.

Shimazaki, K. and P. Somerville (1978). *Bull. Earthq. Res. Inst.* **53**, 613–628.

Smith, S.W. and M. Wyss (1968). *Bull. Seismol. Soc. Am.* **68**, 1955–1974.

Stuart, W.D. (1979). *J. Geophys. Res.* **84**, 1063–1070.

Stuart, W.D. and G. Mavko (1979). *J. Geophys. Res.* **84**, 2153–2160.

Tamura, T., *et al.* (1991). *Geophys. J. Int.* **104**, 507–516.

Thatcher, W. (1983). *J. Geophys. Res.* **88**, 5893–5902.

Tse, S.T. and J.R. Rice (1986). *J. Geophys. Res.* **91**, 9452–9472.

Wolfe, J.E., *et al.* (1981). *Bull. Seismol. Soc. Am.* **71**, 1625–1635.

Wyatt, F.K. (1988). *J. Geophys. Res.* **93**, 7923–7942.

Wyatt F.K., *et al.* (1994). *Bull. Seismol. Soc. Am.* **84**, 768–779.

Wyss, M. and J. Brune (1967). *Bull. Seismol. Soc. Am.* **57**, 1017–1023.

Yamauchi, T. (1987). *J. Phys. Earth* **35**, 19–36.

Editor's Note

Due to space limitations, references with full citation are given in the file "Johnston1FullReferences.tex" on the Handbook CD-ROM, under the directory \36Johnston1. An equivalent PDF file is also provided on the CD.

Please see also Chapter 32, Rock failure and earthquake, by Lockner and Beeler; Chapter 33, State of stress within the Earth, by Ruff; Chapter 34, State of stress in the Earth's lithosphere, by Zoback and Zoback; and Chapter 35, Strength and energetics of active fault zones, by Brune and Thatcher.